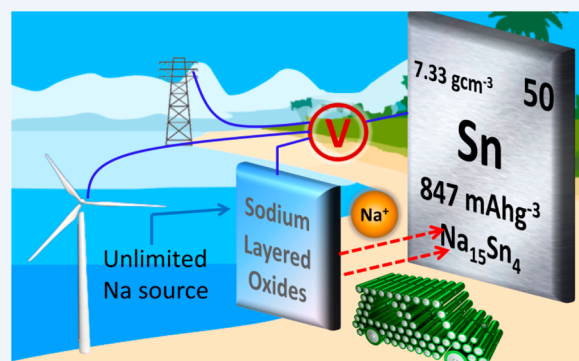# Tin and Tin Compounds for Sodium Ion Battery Anodes: Phase Transformations and Performance

Zhi Li,[†] Jia Ding,[†] and David Mitlin*,[‡,†]

[†]Chemical and Materials Engineering, University of Alberta, Edmonton, Alberta T6G 2V4, Canada
[‡]Chemical & Biomolecular Engineering, Clarkson University, 8 Clarkson Avenue, Potsdam, New York 13699, United States

CONSPECTUS: Sodium ion batteries (NIB, NAB, SIB) are attracting interest as a potentially lower cost alternative to lithium ion batteries (LIB), with readily available and geographically democratic reserves of the metal. Tin is one of most promising SIB anode materials, which alloys with up to 3.75 Na, leading to a charge storage capacity of 847 mAh g^{-1}. In this Account, we outline the state-of-the-art understanding regarding the sodiation-induced phase transformations and the associated performance in a range of Sn-based systems, treating metallic Sn and its alloys, tin oxide (SnO_2), tin sulfide (SnS_2/SnS), and tin phosphide (Sn_4P_3). We first detail what is known about the sodiation sequence in metallic Sn, highlighting the most recent insight into the reactions prior to the terminal equilibrium $Na_{15}Sn_4$ intermetallic. We explain why researchers argue that the equilibrium (phase diagram) series of phase transitions does not occur in this system, and rather why sodiation/desodiation proceeds through a series of metastable crystalline and amorphous structures. We also outline the recent modeling-based insight regarding how this phase transition profoundly influences the mechanical properties of the alloy, progressively changing the bonding and the near neighbor arrangement from "Sn-like" to "Na-like" in the process.

We then go on to discuss the sodiation reactions in SnO_2. We argue that while a substantial amount of experimental work already exists where the focus is on synthesis and testing of tin oxide−based nanocomposites, the exact sodiation sequence is just beginning to be understood. Unlike in Sn and Sn alloys, where capacities near the theoretical are reached at least early during cycling, SnO_2 never quite achieves anything close to the 1398 mAh g^{-1} that would be possible with a combination of fully reversible conversion and alloying reactions. We highlight recent work demonstrating that contrary to general expectations, it is the Sn to $Na_{15}Sn_4$ alloying reaction that is incomplete and hence limits the capacity of the electrode. We also describe how the oxide conversion reaction goes through an intermediate SnO phase, and how its reversibility in a half-cell is highly dependent on the terminal anodic voltage. We then present what is known about sodiation of tin sulfide and of tin phosphide phases, including emerging microstructural evidence that may explain why both the sulfides and the phosphides are unable to achieve their highly promising theoretical capacities under conventional electrode testing conditions. Finally, we provide a broad comparison of the capacity (cycling and rate) performance for a range of Sn based anode materials, and show that there may be indeed an optimum microstructural architecture.

1. INTRODUCTION

Rechargeable sodium ion batteries (NIBs, NABs, SIBs) are emerging as a promising alternative to lithium ion batteries (LIBs) for large-scale stationary applications, perhaps also ultimately penetrating into the transportation sector after additional improvements in performance.[1−10] Sodium offers a much more democratically distributed supply then lithium, being widely available from many sources including seawater. As the cost of Na is more than an order of magnitude lower than of Li (e.g., in 2015, 150 $US/ton vs 3000 $US/ton), there is also a potential for cost reduction associated with presodiated electrodes versus prelithiated ones. Tin is a promising SIB anode material, possessing high charge storage capacity both by weight and by volume.[11] The normally reported maximum capacity is 847 mAh g^{-1}, which is more than 2× that of graphite employed for most commercial LIB anodes. It is also inexpensive

(roughly 20 $US/kg), relatively safe to work with as a powder (not extremely pyrophoric), nontoxic, and highly abundant. An amorphous Sn−Co alloy combined with graphite[12,13] has been employed in commercial Sony Nexelion batteries starting in 2005. While there have been a series of recent excellent reviews broadly covering a range Na ion battery anode and/or cathode materials,[7,14−17] this Account is the first focused topical overview that treats only Sn and Sn compounds, but in significant detail. We believe that this class of materials is promising enough to warrant such attention. In their current state, Sn-based materials in SIBs do not perform as well as Sn in LIBs in any of the key respects (capacity, rate performance, Coulombic efficiency, cycling stability), with a major effort being expanded to both
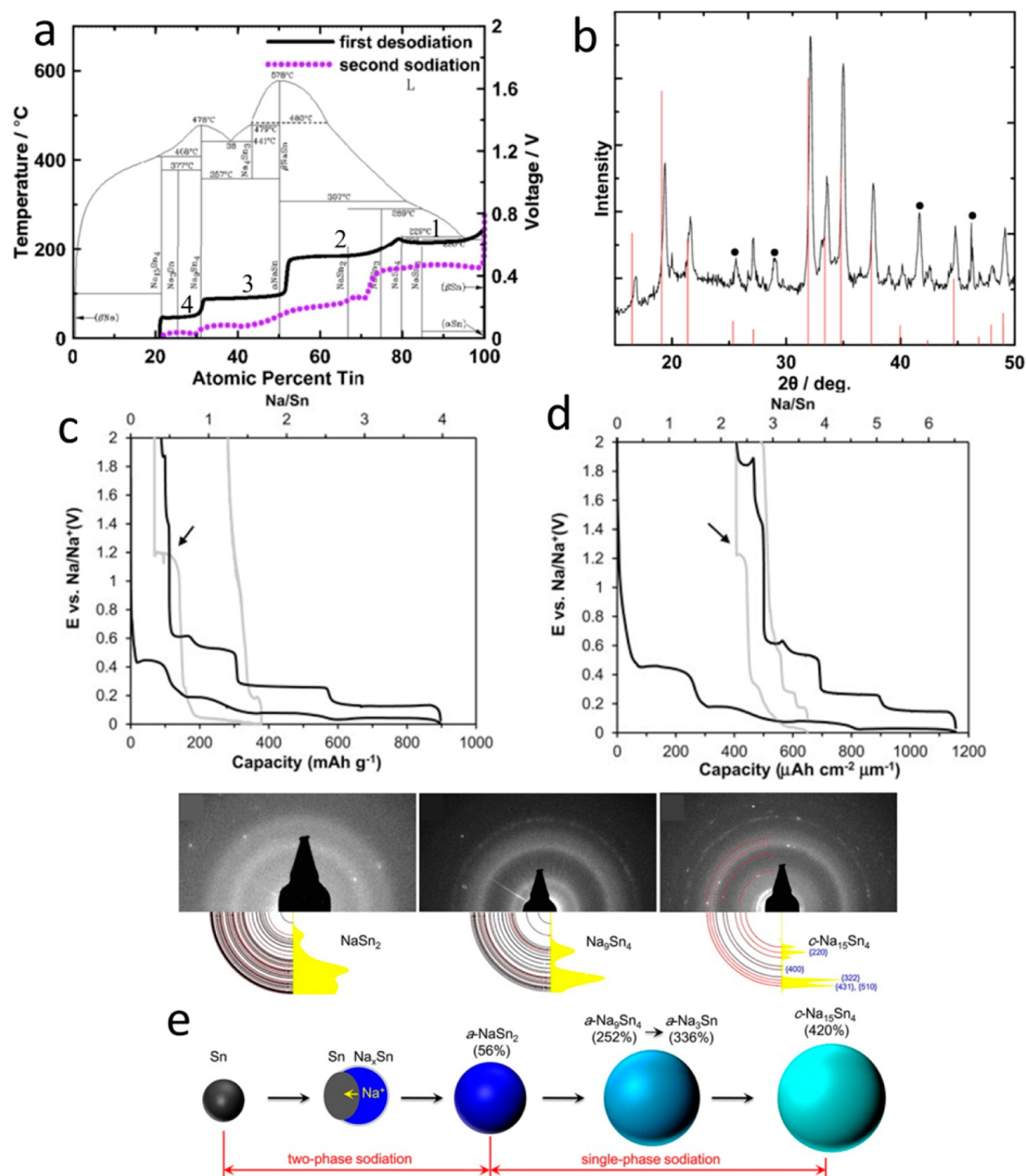
Figure 1. Sodiation behavior metallic Sn. (a) Voltage curves for the 1st desodiation and 2nd sodiation of sputtered Sn, superimposed on the Na−Sn binary phase diagram. (b) In situ XRD pattern of the sodiated phase formed at the end of plateau 3. Expected peak positions and intensities for Na_9Sn_4 are indicated by vertical lines. Peaks from beryllium and cell parts are labeled with black dots. (c, d) Voltage profiles obtained during the first (black) and second (gray) sodiation cycle for "thick" and "thin" Sn film electrodes, respectively. (e) SAD patterns obtained from the in situ TEM study and a schematic illustration showing the structural evolution of Sn nanoparticles during sodiation. Adapted and reproduced with permission from ref 18 (Copyright 2012 Electrochemical Society), ref 23 (Copyright 2013 Elsevier B.V.), and ref 25 (Copyright 2012 American Chemical Society).

create new SIB electrode materials and improve the existing options. All the discussions provided cover electrochemical sodiation at ambient temperature (unless otherwise noted), as little high temperature data is available.

2. METALLIC TIN

The equilibrium Sn−Na phase diagram consists of the following phases at room temperature: $NaSn_6$, $NaSn_4$, $NaSn_3$, $NaSn_2$, Na_9Sn_4, Na_3Sn, and $Na_{15}Sn_4$.[8,18] The crystal structure of Na_9Sn_4 is orthorhombic and that of $Na_{15}Sn_4$ is cubic, whereas the rest are

not fully established. During sodiation of Sn, only the equilibrium terminal intermetallic phase ($Na_{15}Sn_4$, $I\bar{4}3d$) is observed to form, whereas the intermediate intermetallics predicted by the phase diagram[19] do not. For pure Sn and high Sn content alloys, transmission electron microscopy (TEM) shows the $Na_{15}Sn_4$ phase forms as generally spherical nanoparticles, whereas in alloys rich in other elements more complex flake−like morphologies are observed.[20] In pure Sn and Sn-rich alloys (those that effectively behave like pure Sn), during the initial sodiation, there are four sloping plateaus in the ranges of 0.45−

0.41, 0.18−0.15, 0.08−0.06, and 0.03−0.01 V.[8,11,18,21−23] The fact that none of the plateaus are truly flat (they all monotonically decrease) indicates that in each of the associated two-phase regions the system free energy actually evolves with the Na content. During the first desodiation, the plateaus are near 0.15, 0.28, 0.55, and 0.63 V, with the profile in general being less sloped.[8,11,18,21−23] The plateaus become less distinct with cycling, implying further changes to the structure of the intermediate phases.[8,11,18,21−23] The always-observed large hysteresis in the charge/discharge behavior indicates that the sodiation/desodiation transitions are not kinetically facile.[24]

Obrovac et al. performed a series of X-ray analysis based studies to elucidate the intermediate reaction sequence.[18] The charging rate was C/50, based on reported 17 mA/g and a theoretical capacity of 847 mAh g^{-1}. Because of this unusually slow rate and the "bulklike" film thickness, the reported results may not be rigorously applicable for the typical 10−50 nm scale nanomaterials tested at up to 10C or more. Moreover, upon sodiation, the specimens were held at the terminal voltage (0.005 V vs Na/Na$^+$) until the current decreased to 8.5 mAh g^{-1}, which was presumably done to ensure that the equilibrium terminal intermetallic was reached. This is another key difference with what is encountered in most electrode-testing studies, where the current is reversed as soon as the terminal voltage is reached.

Figure 1a shows an overlay of the measured half-cell voltage versus capacity on the equilibrium binary Na−Sn phase diagram.[18,19] Shown are the first and the second sodiation cycle, with the later being of course more representative of a cycling microstructure. During the first cycle there are 4 distinct plateaus, although they do not correlate to the two-phase regions on the equilibrium binary diagram. The X-ray diffraction (XRD) pattern at the conclusion of the fourth plateau corresponded well to the equilibrium Na$_{15}$Sn$_4$ intermetallic, with that pattern being shown in Figure 1b. However, equilibrium intermediate structures were not detected at the end of plateaus 1−3, and no attempt was made to solve for the alternative phases formed. The experimental positions of voltage plateaus did not directly correlate to ab initio modeling of sodiating Sn,[8] which is expected both due to the uncertainty in the equilibrium structure of the intermediate phases, and the kinetic difficulty of nucleation at room temperature.

Recently Veith et al. revisited the intermediate phases formed during the sodiation sequence in Na−Sn.[23] The workers examined "thick" 2 μm and "thin" 100 nm electrodes, showing substantial differences in the quantitative shape of the voltage profiles. The two sets of voltage vs capacity curves are presented in Figure 1c and d. Considering that 100 nm is actually relatively thick for a true "nano" material, one would expect even further deviations from bulk behavior for electrodes that were nanostructured to the 10 nm or less in scale of the Sn phase. It was demonstrated through detailed ex situ XRD analysis that the first plateau was in fact two-distinct plateaus, but with similar free energies. Then the first two-phase region corresponded to β-Sn and a Na$_{0.6}$Sn phase that was crystalline but of undetermined structure. The second two-phase region consisted of crystalline Na$_{0.6}$Sn coexisting with an amorphous Na$_{1.2}$Sn solid solution. Initially a metastable hexagonal ($R\bar{3}m$) Na$_5$Sn$_2$ phase also formed, but becomes suppressed with cycling in the 100 nm films. It is again important to note that the reaction sequence and crystal structures observed even in the 100 nm films may not be what occur at higher charging rates and/or even finer microstructures. For instance, a 1.9 V plateau that is present at low currents is absent at high currents. Also with cycling the

plateaus become less distinct, indicating the many of the phases are kinetically difficult to access.

Wang et al. employed in situ TEM to investigate sodiation of Sn nanoparticles.[25] The authors employed a solid-state in situ cell with Na metal as a counterelectrode and its native oxide as the electrolyte. In such a cell, a high cathodic voltage is employed to drive the Na ions through the native oxide, and the actual voltage on the Sn metal is not known due to the IR drop. The authors did not perform in situ desodiation or cycling, although parallel conventional button half-cell cycling results are reported. Figure 1e shows the proposed sodiation sequence along with the associated indexed diffraction patterns. Tin first sodiates as a crystalline solid solution, followed by a two-phase region where crystalline Sn coexists with an amorphous Sn$_2$Na phase. The authors then reported a single-phase transition of Sn$_2$Na to Na$_9$Sn$_4$ and then to Na$_3$Sn and finally to Na$_9$Sn$_4$. This reaction sequence would generate first a monotonically decreasing voltage vs capacity profile (Sn solid solution), followed by a single plateau (Sn + amorphous Sn$_2$Na), followed again by a monotonically decreasing region. As this is not what is observed during conventional sodiation of button cells, one has to assume that such sequence may have particularities related to the in situ voltage, as well as the differences in electrolyte, direction of sodiation, and so forth.

As shown in the work by Veith et al., the phase sequence also depends on the terminal cutoff voltage.[23] When testing a half-cell, researchers may anodically polarize the working electrode by as much as 3 V. In battery full-cell, the anode discharge (desodiation) voltage window may be substantially narrower. Moreover, the anode charge (sodiation) cutoff voltage may be set to a higher value than the usual 0.01 or 0.02 V vs Na/Na$^+$ employed in half-cell studies. Thus, one should be careful in broadly generalizing the behavior of the above model Sn−Na systems to full cells. We also believe that with additional experimental studies it will become apparent that the exact phase sequence traversed when reaching the terminal alloy composition is microstructural/particle scale, current density, and cycle number dependent.

Shenoy and Medhekar performed first-principles study to explore the sodiation-induced changes in the elastic properties of Sn, along with Pb, Ge, and Si.[26] Simulations demonstrated that sodiation of Sn leads to a 75% decrease in its Young's and shear modulus. Its origin is essentially derived from the changes in the atomic bonding associated with a progressive increase of Na near neighbors to Sn, substituting weaker Sn−Na bonds for Sn−Sn bonds. For example, the intermetallic Na$_{15}$Sn$_4$ is effectively a solid solution of Sn in Na, with all the bonds being between Sn and Na atoms. While the authors simulated the equilibrium crystalline phases, an analogous bond strength transition may be expected for an amorphous solid solution with the same mean composition. One can argue that, on the average, the locally ordered, but long-range disordered Sn−Na solutions will have the same radial distribution of Sn−Na vs Sn−Sn bonds per "unit cell" as their long-range ordered intermetallic counterparts.[27]

The above study has several important implications for the microstructure, mechanical properties, and cycling performance of sodiated Sn. The tremendous drop in the modulus affects the elastic response of the Sn to the stresses associated with volumetric changes during charging/discharging, both intrinsic (inside the material due to nonuniform sodiation) and extrinsic (mismatch with current collector or other phases). Our group's TOF-SIMS and electron energy loss spectroscopy (EELS) TEM study of sodiated of Sn thin films demonstrated distinct

segregation of Na to the highly stressed film—support interface in a fully sodiated half-cell, presumably as a mechanism to soften the interface and relieve the stresses.[20] Going back to the more extensive LIB literature, failure of Si films on Cu supports have been demonstrated to be related to Li segregation in the material, which results in an analogous change in bonding and decrease in elastic properties.[28]

3. TIN OXIDE

Tin dioxide (SnO_2) is perhaps the second most popular emerging Sn-based material for SIB applications.[29−31] A very impressive 1398 mAh g^{-1} is achievable, were SnO_2 to react with Na first through reversible conversion ($SnO_2 + 4Na^+ + 4e^- \leftrightarrow Sn + Na_2O$, 711 mAh g^{-1}), and then through reversible alloying (847 mAh g^{-1}).[18] Even in a half-cell configuration, the experimentally measured capacity of SnO_2 is substantially lower than 1398 mAh g^{-1}.[29,32,33] While it is tempting to attribute this discrepancy to the poor kinetic reversibility of the oxide conversion reaction, there does not seem to be clear data to support this. Oppositely, our group's recent combined TEM, XRD, and X-ray photoelectron spectroscopy (XPS) study of SnO_2 with Na and with Li, detailed the kinetic difficulty of the Na—Sn alloying reaction to the terminal $Na_{15}Sn_4$ intermetallic.[34] With applied voltage a significant portion of the material effectively shuffled between SnO_2 and β crystalline $Sn + Na_2O$. Since in metallic Sn and Sn alloys electrodes there is full sodiation to $Na_{15}Sn_4$, it is concluded that the surrounding oxide conversion product is somehow an impediment. The details of this process are currently not understood. It was however demonstrated that the Na_2O to SnO_2 conversion reaction proceeded through an intermediate crystalline SnO. As this is not the case for the better understood direct conversion of Li_2O to SnO_2, where terminal $Li_{22}Sn_5$ is relatively easily achieved, one may speculate that the two effects are interlinked. For instance SnO may block Na from diffusing into the metallic Sn to a larger extent than would SnO_2. More analytical and modeling work is needed to quantify the impediment mechanism(s). We also showed that the reversibility of the oxide conversion reaction, and hence the electrode capacity, is highly dependent on the terminal anodic voltage in the half-cell. When cycled between voltages more representative of what would be encountered for an anode in a full-cell battery, 0.01 and 1.5 V, the reversible capacity of a SnO_2—carbon nanocomposite was only about 300 mAh g^{-1}, with the crystalline Sn and SnO being the X-ray identifiable phases at 1.5 V. We feel that clearly more analytical and modeling studies are needed to sort out the essential mechanistic details of the combined conversion—alloying sodiation sequence in SnO_2.

In the SnO_2 system there are concerns regarding the low cycle 1 and steady state cycling Coulombic efficiency (CE), although cycling CE has improved though additives such as fluoroethylene carbonate (FEC).[35] It is currently unclear how much of the CE loss is SEI-related, versus based on irreversible trapping of Na in bulk of Sn metal and/or oxide. Our own work showed a comparable CE loss at two substantially different tin oxide particulate sizes (surface areas), suggesting that irreversible Na trapping in the bulk is indeed important.[36,37] It is believed that again more systematic analytical work is essential, in this case to conclusively elucidate bulk vs surface Na trapping.

4. TIN SULFIDE

Tin sulfide[38−42] and tin phosphide[43−45] based anodes are receiving increasing scientific attention. Sn sulfide can theoret-

ically combine the well-known Na−S conversion reaction with an alloying reaction to yield a high capacity anode that effectively operates as a S−Na and Sn−Na nanocomposite (the SnS_2 does not reform upon desodiation). For hexagonal SnS_2, the reactions are the following: $SnS_2 + 4Na \rightarrow Sn + 2Na_2S$ and $Sn + 3.75Na \rightarrow Na_{15}Sn_4$, yielding a reversible capacity of 1,137 mAh g^{-1}. With the orthorhombic SnS phase the reaction sequence is analogous: $SnS + 2Na \rightarrow Sn + Na_2S$ and $Sn + 3.75Na \rightarrow Na_{15}Sn_4$, but with a theoretical capacity of 1022 mAh g^{-1}.

An excellent comparison of the performance of the two sulfide systems was recently published by Guo et al.[39] The authors employed a tin sulfide @ graphene architecture and demonstrated that with both materials the sulfide decomposes to metallic Sn, which is consequently alloyed to form the $Na_{15}Sn_4$ intermetallic. In the case of SnS, the decomposed Sn phase had a diamond cubic crystal structure (low temperature α-tin). In the case of SnS_2, the decomposed Sn phase had a tetragonal crystal structure (metallic β-tin). Based on the electrochemical CV profiles, the authors argued that the SnS phase is reformed during desodiation, while SnS_2 remains permanently decomposed. However, the ex situ XRD patterns collected during the first desodiation did not display the characteristic SnS Bragg reflections, rather showing clear S and Sn (separate analysis) signals. These results are presented in Figure 2. In our opinion,
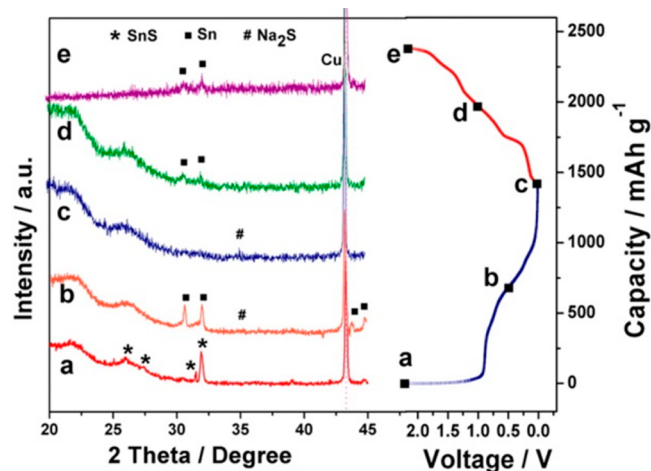
Figure 2. XRD patterns of the SnS@graphene electrode collected at various stages of sodiation, marked in the corresponding voltage profile: (a) fresh electrode, (b) first sodiation to 0.5 V, (c) first sodiation to 0.01 V, (d) first desodiation to 1.0 V, and (e) first desodiation to 2.2 V. Reprinted with permission from ref 39. Copyright 2014 American Chemical Society.

more analytical work is needed to address the question of the reversibility of the SnS and SnS_2 reactions. If the Sn sulfide phase(s) do reform during desodiation, they would do so at the nanoscale and are highly likely to be at least in part amorphous. This makes it difficult to extract phase information even from the most careful XRD experiments, with additional techniques such as HRTEM, EELS, and XPS being essential for identification. Certainly there may also be a situation where the tin sulfide is partially reformed, with a portion of the microstructure remaining metallic Sn.

It is difficult to ascertain the exact Sn—sulfide capacity, since the systems employed inevitably also contain a substantial mass fraction of a Na active carbon phase, such as reduced graphene. In general, it appears that the capacities are always below the theoretical, even if the mass fraction of the carbon phases is
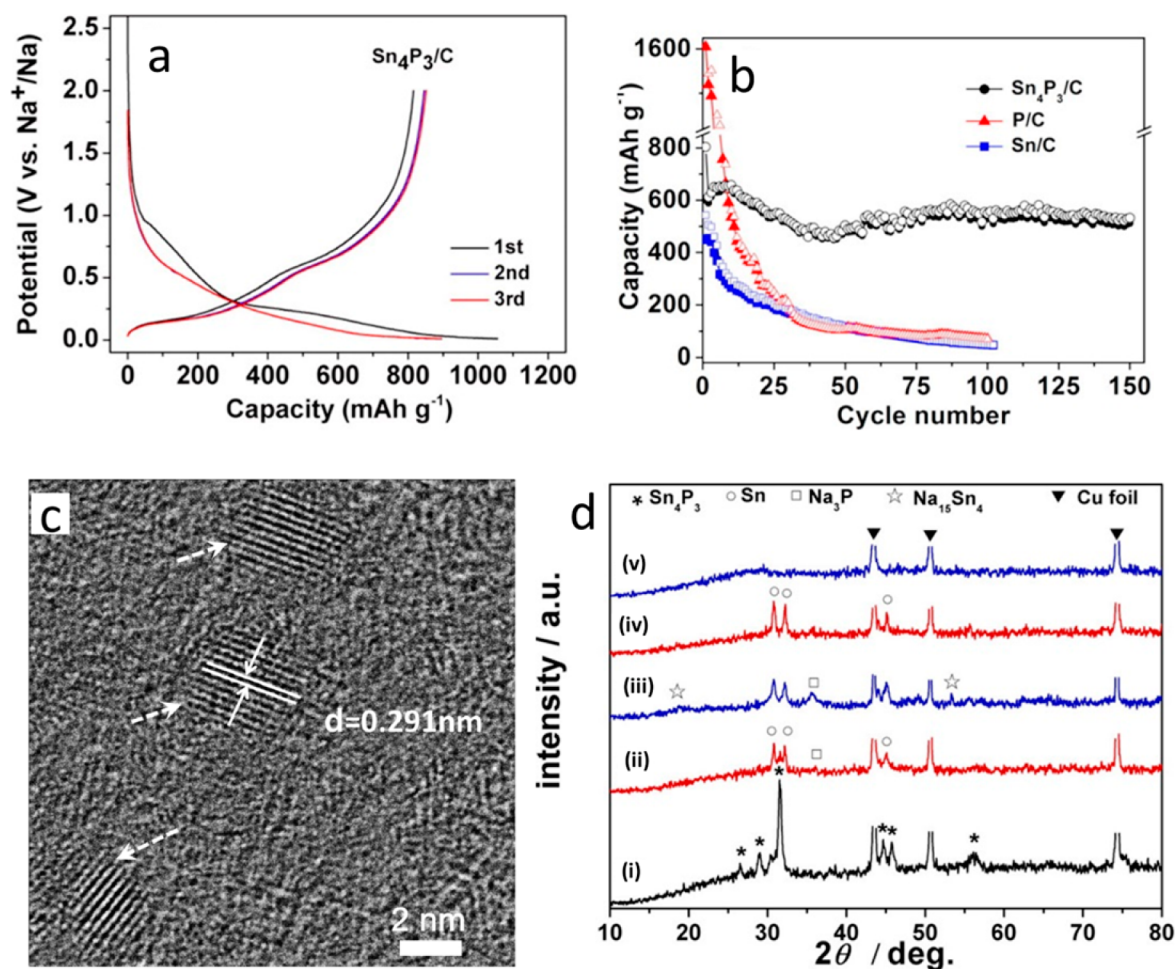
Figure 3. Sn_4P_3/C nanocomposites as NIB anodes. (a) First sodiation/desodiation curves at 50 mA g^{-1}. (b) Comparison of the reversible capacities of the Sn_4P_3/C, Sn/C, and P/C electrodes, tested at 100 mA g^{-1}. (c) HRTEM micrograph of the Sn_4P_3/C after the first sodiation/desodiation. (d) XRD patterns of the Sn4P3/C electrode at different voltage states: (i) fresh electrode; (ii) first sodiation to 0.25 V; (iii) first sodiation to 0.01 V; (iv) after first desodiation to 0.5 V; and (v) first desodiation to 2.0 V. All panels reprinted with permission from ref 44. Copyright 2014 American Chemical Society.

accounted for in the calculation. Similarly to the case of SnO_2, having the Sn be surrounded by a conversion product may have a negative influence on its alloying sodiation kinetics. For instance, a Li_2S sheath may block the diffusion of Na into the Sn, or create strain that opposed the alloying-induced expansion. In the authors' opinion, more work is needed to establish the full reaction sequence for the Sn–S system. The S–Na system is quite new, and does not to have the same levels of understanding of the intermediate polysulfide species as does S–Li. The Sn–S–Na system may well display the polysulfide shuttling problem, well-known for Li–S batteries, resulting in early capacity fade. No model "pure" Na–Sn–S have been tested to date. The electrodes so far employed contain a considerable amount of secondary carbon, which may also pin soluble polysulfide anions similarly to its action in Li–S.[46,47]

5. TIN PHOSPHIDE

The tin–phosphide system is another promising conversion plus alloying material,[43−45] with a theoretical capacity of 1132 mAh g^{-1} for Sn_4P_3. The system also offers the key advantage of having the majority of the capacity in the useful voltage range of below 0.5 V vs Na/Na$^+$. An interesting study on this material was recently published by Qian et al.[44] Their galvanostatic charge–discharge curves are presented in Figure 3a, with the cycling results being presented in Figure 3b. The theoretical capacity of 1132 mAh g^{-1}, which corresponds to sodiation of P to the terminal Na_3P and of Sn to the terminal $Na_{15}Sn_4$, was never achieved. Rather the maximum reversible desodiation capacity was about 850 mAh g^{-1}. Figure 3c shows a HRTEM image of Sn_4P_3/C after a single sodiation–desodiation process. The system was both highly dispersed and interconnected, with typical crystallite size of 2−5 nm embedded in an amorphous matrix. As will be discussed later in this Account, this type of microstructure appears to be ideal for achieving optimum cycling and rate capability. The authors identified the spacing of the lattice fringes in the crystalline phase to be that of metallic Sn. We believe that it is necessary to additionally provide indexed zone-axis FFTs and/or SAD patterns in order conclusively identify the final structure. This is especially the case since the XRD pattern of the desodiated material does not yield any Bragg peaks besides from the Cu support, as shown in Figure 3d.

The reaction sequence was proposed to be the following: $Sn_4P_3 + 24Na^+ + 24e^- \rightarrow Na_{15}Sn_4 + 3Na_3P$ during the initial sodiation. The authors argued that upon subsequent desodiation the Sn_4P_3 phase is not reformed, which in our opinion is correct based on the expected sluggish solid-state interdiffusion kinetics of Sn–P. Rather the material then begins to behave as a true nanocomposite, with the Sn and the P sodiating and desodiating separately: $Na_{15}Sn_4 \leftrightarrow 4Sn + 15Na^+ + 15e^-$, $Na_3P \leftrightarrow P + 3Na^+ +$

Table 1. Summary of the state-of-the-art Sn and Sn compounds based electrodes materials for SIB applications

material	synthesis method	potential (V)	first charge capacity (mAh g^{-1} (A/g))^a	capacity after (x) cycles (mAh g^{-1})	CE in first Cycle	capacity at high rate (mAh g^{-1} (A/g))^a	additive	ref
Sn/porous C composite	thermal reduction	0.02–1.5	295(0.02)	195(15)	38.8%	200(0.2); 100(0.4); 75(1)	CMC^b	5
Sn film on natural wood fiber	electrodeposition	0.005–1.5	339(0.084)	145(400)	23%	200(0.084); 130(0.168); 50(0.84)	NA	51
Al$_2$O$_3$/SnNPs@CNF	electrospinning-ALD	0.02–1.5	625(0.0847)	650(40)	63.7%	NA	NA	53
Sn/graphite composite	ball milling	0.01–1.2	410(0.05)	360(20)	70%	NA	NA	54
SnO thick film	gas-deposition	0.005–2	580*(0.05)	250*(50)	56%	200(0.5); 120(1)	NA	55
SnO$_2$@MWCNT composite	solvothermal	0.01–2	480(0.07)	350(50)	57.2%	350(0.133); 210(0.333)	NA	32
octahedral SnO$_2$ NP	hydrothermal	0.01–3	450(0.02)	420(100)	25.4%	200(0.16)	NA	33
SnO$_2$@graphene composite	hydrothermal	0.01–3	600*(0.02)	638(100)	30%	302(0.16); 263(0.32); 143(0.64)	NA	52
SnO$_2$@RGO composite	hydrothermal	0.005–2.5	407(0.1)	330(150)	33%	250(0.2); 180 (0.5); 120(1)	PAA,^{c} FEC^d	30
SnS nanorods	hydrolysis-annealing	0.1–2	475(0.125)	350*(30)	61.3%	400(0.5); 300(1)	sodium alginate	42
layered SnS$_2$-on RGO	hydrothermal	0.01–2.5	630(0.2)	628 (100)	75%	610*(0.5); 590*(1) ; 544* (2)	NA	41
SnS graphene nanocomposite	hydrothermal	0–3	1050*(0.03)	947 (50)	73%	525(0.81); 450(2.43); 300(7.29)	FEC^d	39
exfoliated SnS$_2$ on graphene	Li assisted exfoliation-hydrothermal	0.01–2.5	864.5(0.2)	610*(100)	69%	532(0.5); 461(1); 381 (2); 326(4)	CMC^b	40
Sn$_4$P$_3$ microparticles	ball milling	0–1.5	680*(0.1)	520*(150)	77.3%	NA	FEC,^{d} PAA^c	43
Sn$_4$P$_3$/C nanocomposite	ball milling	0–2	816(0.05)		77.3%	435 (0.5); 349 (1)	FEC,^{d} CMC^b	44
Sn–Ni intermetallic microcages	solvothermal	0.01–2	384 (0.6)	280(300)	35.5%	447 (1.2); 351 (3); 276 (6)	NA	48

^{a}Capacity at a certain current density (in brackets). Capacities marked with an asterisk (*) are based on best estimate from the published figures. ^{b}Carboxymethyl cellulose. ^{c}Poly(acrylic acid). ^{d}Fluoroethylene carbonate.

3e$^-$. According to the authors who also performed baseline experiments on Sn–C, the P acts as a matrix that prevents agglomeration of Sn. The XRD results presented in Figure 3d show what appears to be a general trend for Sn-based conversion + alloying systems, including our own work on SnO$_2$.[34] First, the initially present Sn compound does reform after desodiation; that is, the system remains decomposed. Second, the Na conversion reaction appears to proceed further than the Sn alloying reaction. Examining the XRD profiles presented for the once sodiated and then desodiated Sn$_4$P$_3$, one observes no evidence of this phase being reversible upon desodiation to 2.2 V (curve labeled "v"). At 0.01 V there is clear evidence of crystalline Na$_3$P and crystalline Sn, with only a minor Na$_{15}$Sn$_4$ peak being present. This strongly suggests that the limiting sodiation reaction is the solid-state alloying of Sn by Na, rather than the conversion reaction between Sn and P. Analogous XRD findings regarding the absence Na$_{15}$Sn$_4$ Bragg peaks were published at the same time period by Lee et al.[43] From this vantage, the Na–Sn system is distinct from Li–Sn, where the theoretical capacity is often reached during the early cycles.[48,49]

6. MICROSTRUCTURE–PERFORMANCE RELATIONS

Here we will provide a comparison for a range of high performance Sn-based SIB anode materials. Table 1 provides examples of a diverse microstructures, with and without secondary phases additions.[5,32,33,42,50–55] Regretfully, we are unable to discuss all the previous findings within the limited space of this Account. Almost all high performance electrodes are nano rather than micro in their phase distribution, particle

dimensions, and so forth. Microscale SnO$_2$ shows limited cycle life,[55] a feature common to micro- and macroscale alloying and conversion particulates.[29,33] Materials such as SnO$_2$-based nanowires or nanoparticles, which do not contain a secondary supporting phase, also possess long-term cycling limitations. Overall it appears that "2D" phases such as graphene may outperform the "1D" materials such as CNTs.[5,30,32,51,52]

The expansion of pure Sn upon alloying to the terminal Na$_{15}$Sn$_4$ is a colossal 420%, which is substantially higher than the 260% associated with the formation of Li$_{22}$Sn$_5$. For Sn-based alloys, this expansion may also be very high, such as upward of 300% for the Sn–Ge–Sb system.[20] Without a secondary matrix to deal with this expansion, the Sn electrode will quickly decrepitate and loose electrical contact during cycling. In classic Li ion battery terms, such a matrix should "mechanically buffer" the sodiation expansion. Of course the volumetric expansion associated Sn alloying and any conversion reactions must not be prevented, as sodiation would not occur if it were. However, with a highly elastically compliant scaffold the electrode would be able to reversibly "breathe" during sodiation/desodiation and thus last for a much higher number of cycles.[51] A thin and highly Na active matrix, such nm-scale nongraphitic carbon, should also allow for a high Na flux during charge/discharge.

Figure 4 shows several examples of successful strategies to create nanocomposites with superior rate and cycling performance. Authors employed viral nanoforests[56] (Figure 4a), wood fibers[51] (Figure 4b), graphene[38] (Figure 4c), and 3D graphene aerogel[36] (Figure 4d) to improve the performance of Sn, SnS$_2$, and SnO$_2$ anodes. From these and other studies,[30,32,34] we argue
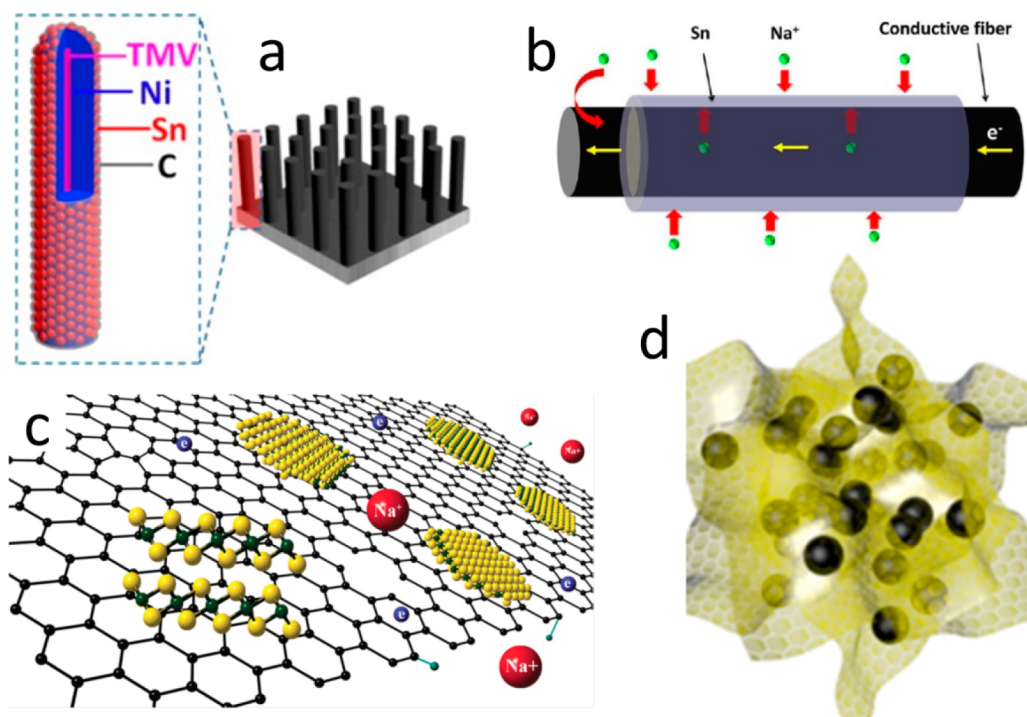
Figure 4. Schematic illustrations of several Sn-based NIB anode nanocomposites with outstanding electrochemical performance. (a) Tin-coated viral nanoforests. (b) Tin supported on carbonized cellulose fibers derived from wood. (c) Few layered SnS_2 supported on reduced graphene. (d) SnO_2 aerogel trapped in 3D graphene aerogels. Reprinted with permission from ref 56 (Copyright 2013 American Chemical Society), ref 51 (Copyright 2013 American Chemical Society), and ref 41 (Copyright 2015 Wiley).

that an ideal Sn SIB microstructure contains a Na-active, highly electrically conductive secondary matrix. An interconnected array, rather than individual platelets, would minimize electrical losses associated with the usual contact points between particles and would thus aid rate capability. Ideally, this secondary phase will at least partially encapsulate the Sn, thus stabilizing the long-term cycling behavior by both reducing the associated microstructural coarsening and preventing any electrical contact loss.

As solid-state diffusion is often the rate-limiting step in the sodiation processes, the active particle size will be another key feature in establishing electrode performance, especially its rate capability. Judging from past literature, it appears that having the Sn phase be truly nanoscale is essential.[23,30,36] Overall, microstructures with 10 nm and sub-10 nm Sn-based particles outperform their coarser 50 or 100 nm counterparts. This is a consistent trend in various studies where a coarser baseline was tested identically.[23,34] Solid-state diffusion time may be estimated as the following: $\tau \approx l^2/D$, where τ is the characteristic time constant, l is the diffusion length, and D is the diffusion coefficient. Thus, the time to sodiation will scale quadratically with material dimensions: $\tau = 5$ s for a 10 nm radius particulate, it will be 20 s for a particulate twice as large, and so forth.

7. SUMMARY

The Account focused on tin, tin oxide, tin sulfides, and tin phosphides for sodium ion battery (NIB, NAB, SIB) anode applications. These materials are quite "young" in respect to being tested against Na, with the current understanding of the reaction sequence being not fully mature. Our focus was to explain what is currently known and to outline the gaps. We also provide a performance survey of published materials and provide what we believe are general microstructural design guidelines for optimizing parameters such as cycling life and rate capability.

■ AUTHOR INFORMATION

Corresponding Author

*E-mail: dmitlin@clarkson.edu.

Notes

The authors declare no competing financial interest.

Biographies

Zhi Li received his Ph.D. in 2009 from Colorado School of Mines. He joined the University of Alberta as a postdoctoral research fellow in 2010. His research interests are in the field of nanomaterials for catalysis and energy storage, where he has published 29 research papers with more than 1000 citations. He also holds a M.S. in Engineering and Technology Management, specialized in strategy and innovation. Zhi is passionate in both development and commercialization of low-cost nanotechnologies as solutions to the energy crisis and climate change.

Jia Ding is a Ph.D. candidate of the Department of Chemical and Materials Engineering at University of Alberta under the supervision of Prof. David Mitlin. He received a B.S. from Huazhong University of Sciences and Technology (2009), China, and M.S. degree in Materials Science from Chinese Academy of Sciences (2012), China. He has published 14 peer-reviewed journal articles. His research in UofA is focusing on advanced carbon and metal oxide based materials design and fabrication as electrodes for Li/Na ion batteries and capacitors.

David Mitlin is a Professor and GE Chair in Oil and Gas Systems at Clarkson University, jointly in the Departments of Chemical & Biomolecular Engineering and Mechanical Engineering. He has published over 125 peer-reviewed journal articles and has presented over 60 invited or keynote talks. Prof. Mitlin also holds 3 U.S. patents, is an Editor for Journal of Materials Science and serves on the Board of Review for Metallurgical and Materials Transactions. Most importantly, he has supervised and graduated 13 Ph.D. students, 6 M.S. students, and

8 post docs, all of who are now working as leaders in industry, government research organizations, and academia. Dave received a Doctorate in Materials Science from U.C. Berkeley in 2000.

■ REFERENCES

(1) Slater, M. D.; Kim, D.; Lee, E.; Johnson, C. S. Sodium-Ion Batteries. *Adv. Funct. Mater.* **2013**, *23*, 947−958.

(2) Ellis, B. L.; Nazar, L. F. Sodium and sodium-ion energy storage batteries. *Curr. Opin. Solid State Mater. Sci.* **2012**, *16*, 168−177.

(3) Palomares, V.; Serras, P.; Villaluenga, I.; Hueso, K. B.; Carretero-Gonzalez, J.; Rojo, T. Na-ion batteries, recent advances and present challenges to become low cost energy storage systems. *Energy Environ. Sci.* **2012**, *5*, 5884−5901.

(4) Xiao, L.; Cao, Y.; Xiao, J.; Wang, W.; Kovarik, L.; Nie, Z.; Liu, J. High capacity, reversible alloying reactions in SnSb/C nanocomposites for Na-ion battery applications. *Chem. Commun.* **2012**, *48*, 3321−3323.

(5) Xu, Y.; Zhu, Y.; Liu, Y.; Wang, C. Electrochemical Performance of Porous Carbon/Tin Composite Anodes for Sodium-Ion and Lithium-Ion Batteries. *Adv. Energy Mater.* **2013**, *3*, 128−133.

(6) Kim, S.-W.; Seo, D.-H.; Ma, X.; Ceder, G.; Kang, K. Electrode Materials for Rechargeable Sodium-Ion Batteries: Potential Alternatives to Current Lithium-Ion Batteries. *Adv. Energy Mater.* **2012**, *2*, 710−721.

(7) Palomares, V.; Casas-Cabanas, M.; Castillo-Martinez, E.; Han, M. H.; Rojo, T. Update on Na-based battery materials. A growing research path. *Energy Environ. Sci.* **2013**, *6*, 2312−2337.

(8) Chevrier, V. L.; Ceder, G. Challenges for Na-ion Negative Electrodes. *J. Electrochem. Soc.* **2011**, *158*, A1011−A1014.

(9) Pan, H.; Hu, Y.-S.; Chen, L. Room-temperature stationary sodium-ion batteries for large-scale electric energy storage. *Energy Environ. Sci.* **2013**, *6*, 2338−2360.

(10) Bommier, C.; Ji, X. Recent Development on Anodes for Na-Ion Batteries. *Isr. J. Chem.* **2015**, *55*, 486−507.

(11) Kim, H.; Jeong, G.; Kim, Y.-U.; Kim, J.-H.; Park, C.-M.; Sohn, H.-J. Metallic anodes for next generation secondary batteries. *Chem. Soc. Rev.* **2013**, *42*, 9011−9034.

(12) Dahn, J. R.; Mar, R. E.; Abouzeid, A. Combinatorial Study of Sn$_{1−x}$Co$_x$ (0 < *x* < 0.6) and [Sn$_{0.55}$Co$_{0.45}$]$_{1−y}$C$_y$ (0 < *y* < 0.5) Alloy Negative Electrode Materials for Li-Ion Batteries. *J. Electrochem. Soc.* **2006**, *153*, A361−A365.

(13) Hassoun, J.; Mulas, G.; Panero, S.; Scrosati, B. Ternary Sn−Co−C Li-ion battery electrode material prepared by high energy ball milling. *Electrochem. Commun.* **2007**, *9*, 2075−2081.

(14) Han, M. H.; Gonzalo, E.; Singh, G.; Rojo, T. A comprehensive review of sodium layered oxides: powerful cathodes for Na-ion batteries. *Energy Environ. Sci.* **2015**, *8*, 81−102.

(15) Yabuuchi, N.; Kubota, K.; Dahbi, M.; Komaba, S. Research Development on Sodium-Ion Batteries. *Chem. Rev.* **2014**, *114*, 11636−11682.

(16) Hong, S. Y.; Kim, Y.; Park, Y.; Choi, A.; Choi, N.-S.; Lee, K. T. Charge carriers in rechargeable batteries: Na ions vs. Li ions. *Energy Environ. Sci.* **2013**, *6*, 2067−2081.

(17) Kundu, D.; Talaie, E.; Duffort, V.; Nazar, L. F. The Emerging Chemistry of Sodium Ion Batteries for Electrochemical Energy Storage. *Angew. Chem., Int. Ed.* **2015**, *54*, 3431−3448.

(18) Ellis, L. D.; Hatchard, T. D.; Obrovac, M. N. Reversible Insertion of Sodium in Tin. *J. Electrochem. Soc.* **2012**, *159*, A1801−A1805.

(19) Massalski, T. B.; Okamoto, H.; Subramanian, P.; Kacprzak, L.; Scott, W. W. *Binary alloy phase diagrams*; American Society for Metals: Materials Park, OH, 1986; Vol. 1.

(20) Farbod, B.; Cui, K.; Kalisvaart, W. P.; Kupsta, M.; Zahiri, B.; Kohandehghan, A.; Lotfabad, E. M.; Li, Z.; Luber, E. J.; Mitlin, D. Anodes for sodium ion batteries based on tin-germanium-antimony alloys. *ACS Nano* **2014**, *8*, 4415−4429.

(21) Baggetto, L.; Jumas, J.-C.; Gorka, J.; Bridges, C. A.; Veith, G. M. Predictions of particle size and lattice diffusion pathway requirements for sodium-ion anodes using [small eta]-Cu6Sn5 thin films as a model system. *Phys. Chem. Chem. Phys.* **2013**, *15*, 10885−10894.

(22) Lin, Y.-M.; Abel, P. R.; Gupta, A.; Goodenough, J. B.; Heller, A.; Mullins, C. B. Sn−Cu Nanocomposite Anodes for Rechargeable Sodium-Ion Batteries. *ACS Appl. Mater. Interfaces* **2013**, *5*, 8273−8277.

(23) Baggetto, L.; Ganesh, P.; Meisner, R. P.; Unocic, R. R.; Jumas, J.-C.; Bridges, C. A.; Veith, G. M. Characterization of sodium ion electrochemical reaction with tin anodes: Experiment and theory. *J. Power Sources* **2013**, *234*, 48−59.

(24) Christian, J. The theory of transformations in metals and alloys. *Mater. Today* **2003**, *6*, 53.

(25) Wang, J. W.; Liu, X. H.; Mao, S. X.; Huang, J. Y. Microstructural Evolution of Tin Nanoparticles during In Situ Sodium Insertion and Extraction. *Nano Lett.* **2012**, *12*, 5897−5902.

(26) Mortazavi, M.; Deng, J.; Shenoy, V. B.; Medhekar, N. V. Elastic softening of alloy negative electrodes for Na-ion batteries. *J. Power Sources* **2013**, *225*, 207−214.

(27) Egami, T.; Billinge, S. J.: *Underneath the Bragg peaks: structural analysis of complex materials*; Elsevier, 2003; Vol. 16.

(28) Stournara, M. E.; Xiao, X.; Qi, Y.; Johari, P.; Lu, P.; Sheldon, B. W.; Gao, H.; Shenoy, V. B. Li Segregation Induces Structure and Strength Changes at the Amorphous Si/Cu Interface. *Nano Lett.* **2013**, *13*, 4759−4768.

(29) Park, J.; Park, J.-W.; Han, J.-H.; Lee, S.-W.; Lee, K.-Y.; Ryu, H.-S.; Kim, K.-W.; Wang, G.; Ahn, J.-H.; Ahn, H.-J. Charge−discharge properties of tin dioxide for sodium-ion battery. *Mater. Res. Bull.* **2014**, *58*, 186−189.

(30) Wang, Y.-X.; Lim, Y.-G.; Park, M.-S.; Chou, S.-L.; Kim, J. H.; Liu, H.-K.; Dou, S.-X.; Kim, Y.-J. Ultrafine SnO2 nanoparticle loading onto reduced graphene oxide as anodes for sodium-ion batteries with superior rate and cycling performances. *J. Mater. Chem. A* **2014**, *2*, 529−534.

(31) Gu, M.; Kushima, A.; Shao, Y.; Zhang, J.-G.; Liu, J.; Browning, N. D.; Li, J.; Wang, C. Probing the Failure Mechanism of SnO2 Nanowires for Sodium-Ion Batteries. *Nano Lett.* **2013**, *13*, 5203−5211.

(32) Wang, Y.; Su, D.; Wang, C.; Wang, G. SnO$_2$@MWCNT nanocomposite as a high capacity anode material for sodium-ion batteries. *Electrochem. Commun.* **2013**, *29*, 8−11.

(33) Su, D.; Wang, C.; Ahn, H.; Wang, G. Octahedral tin dioxide nanocrystals as high capacity anode materials for Na-ion batteries. *Phys. Chem. Chem. Phys.* **2013**, *15*, 12543−12550.

(34) Ding, J.; Li, Z.; Wang, H. L.; Cui, K.; Kohandehghan, A.; Tan, X. H.; Karpuzov, D.; Mitlin, D. Sodiation vs. lithiation phase transformations in a high rate - high stability SnO2 in carbon nanocomposite. *J. Mater. Chem. A* **2015**, *3*, 7100−7111.

(35) Dai, K.; Zhao, H.; Wang, Z.; Song, X.; Battaglia, V.; Liu, G. Toward high specific capacity and high cycling stability of pure tin nanoparticles with conductive polymer binder for sodium ion batteries. *J. Power Sources* **2014**, *263*, 276−279.

(36) Li, Z.; Ding, J.; Wang, H.; Cui, K.; Stephenson, T.; Karpuzov, D.; Mitlin, D. High Rate SnO$_2$ - Graphene Dual Aerogel Anodes and their Kinetics of Lithiation and Sodiation. *Nano Energy* **2015**, *15*, 369−378.

(37) Ding, J.; Wang, H.; Li, Z.; Cui, K.; Karpuzov, D.; Tan, X.; Kohandehghan, A.; Mitlin, D. Peanut shell hybrid sodium ion capacitor with extreme energy−power rivals lithium ion capacitors. *Energy Environ. Sci.* **2015**, *8*, 941−955.

(38) Zhang, Y.; Zhu, P.; Huang, L.; Xie, J.; Zhang, S.; Cao, G.; Zhao, X. Few-Layered SnS$_2$ on Few-Layered Reduced Graphene Oxide as Na-Ion Battery Anode with Ultralong Cycle Life and Superior Rate Capability. *Adv. Funct. Mater.* **2015**, *25*, 481−489.

(39) Zhou, T.; Pang, W. K.; Zhang, C.; Yang, J.; Chen, Z.; Liu, H. K.; Guo, Z. Enhanced Sodium-Ion Battery Performance by Structural Phase Transition from Two-Dimensional Hexagonal-SnS$_2$ to Orthorhombic-SnS. *ACS Nano* **2014**, *8*, 8323−8333.

(40) Liu, Y.; Kang, H.; Jiao, L.; Chen, C.; Cao, K.; Wang, Y.; Yuan, H. Exfoliated-SnS$_2$ restacked on graphene as a high-capacity, high-rate, and long-cycle life anode for sodium ion batteries. *Nanoscale* **2015**, *7*, 1325−1332.

(41) Qu, B.; Ma, C.; Ji, G.; Xu, C.; Xu, J.; Meng, Y. S.; Wang, T.; Lee, J. Y. Layered SnS$_2$-Reduced Graphene Oxide Composite − A High-Capacity, High-Rate, and Long-Cycle Life Sodium-Ion Battery Anode Material. *Adv. Mater.* **2014**, *26*, 3854−3859.

(42) Dutta, P. K.; Sen, U. K.; Mitra, S. Excellent electrochemical performance of tin monosulphide (SnS) as a sodium-ion battery anode. *RSC Adv.* **2014**, *4*, 43155−43159.

(43) Kim, Y.; Kim, Y.; Choi, A.; Woo, S.; Mok, D.; Choi, N.-S.; Jung, Y. S.; Ryu, J. H.; Oh, S. M.; Lee, K. T. Tin Phosphide as a Promising Anode Material for Na-Ion Batteries. *Adv. Mater.* **2014**, *26*, 4139−4144.

(44) Qian, J.; Xiong, Y.; Cao, Y.; Ai, X.; Yang, H. Synergistic Na-Storage Reactions in Sn_4P_3 as a High-Capacity, Cycle-Stable Anode of Na-Ion Batteries. *Nano Lett.* **2014**, *14*, 1865−1869.

(45) Li, W.; Chou, S.-L.; Wang, J.-Z.; Kim, J. H.; Liu, H.-K.; Dou, S.-X. $Sn_{4+x}P_3$ @ Amorphous Sn-P Composites as Anodes for Sodium-Ion Batteries with Low Cost, High Capacity, Long Life, and Superior Rate Capability. *Adv. Mater.* **2014**, *26*, 4037−4042.

(46) Ji, X.; Lee, K. T.; Nazar, L. F. A highly ordered nanostructured carbon-sulphur cathode for lithium-sulphur batteries. *Nat. Mater.* **2009**, *8*, 500−506.

(47) Zhang, B.; Qin, X.; Li, G. R.; Gao, X. P. Enhancement of long stability of sulfur cathode by encapsulating sulfur into micropores of carbon spheres. *Energy Environ. Sci.* **2010**, *3*, 1531−1537.

(48) Liu, J.; Wen, Y.; van Aken, P. A.; Maier, J.; Yu, Y. Facile Synthesis of Highly Porous Ni−Sn Intermetallic Microcages with Excellent Electrochemical Performance for Lithium and Sodium Storage. *Nano Lett.* **2014**, *14*, 6387−6392.

(49) Qin, J.; He, C.; Zhao, N.; Wang, Z.; Shi, C.; Liu, E.-Z.; Li, J. Graphene Networks Anchored with Sn@Graphene as Lithium Ion Battery Anode. *ACS Nano* **2014**, *8*, 1728−1738.

(50) Chen, W.; Deng, D. Deflated Carbon Nanospheres Encapsulating Tin Cores Decorated on Layered 3-D Carbon Structures for Low-Cost Sodium Ion Batteries. *ACS Sustainable Chem. Eng.* **2014**, *3*, 63−70.

(51) Zhu, H.; Jia, Z.; Chen, Y.; Weadock, N.; Wan, J.; Vaaland, O.; Han, X.; Li, T.; Hu, L. Tin Anode for Sodium-Ion Batteries Using Natural Wood Fiber as a Mechanical Buffer and Electrolyte Reservoir. *Nano Lett.* **2013**, *13*, 3093−3100.

(52) Su, D.; Ahn, H.-J.; Wang, G. SnO_2@graphene nanocomposites as anode materials for Na-ion batteries with superior electrochemical performance. *Chem. Commun.* **2013**, *49*, 3131−3133.

(53) Han, X.; Liu, Y.; Jia, Z.; Chen, Y.-C.; Wan, J.; Weadock, N.; Gaskell, K. J.; Li, T.; Hu, L. Atomic-Layer-Deposition Oxide Nanoglue for Sodium Ion Batteries. *Nano Lett.* **2013**, *14*, 139−147.

(54) Datta, M. K.; Epur, R.; Saha, P.; Kadakia, K.; Park, S. K.; Kumta, P. N. Tin and graphite based nanocomposites: Potential anode for sodium ion batteries. *J. Power Sources* **2013**, *225*, 316−322.

(55) Shimizu, M.; Usui, H.; Sakaguchi, H. Electrochemical Na-insertion/extraction properties of SnO thick-film electrodes prepared by gas-deposition. *J. Power Sources* **2014**, *248*, 378−382.

(56) Liu, Y.; Xu, Y.; Zhu, Y.; Culver, J. N.; Lundgren, C. A.; Xu, K.; Wang, C. Tin-Coated Viral Nanoforests as Sodium-Ion Battery Anodes. *ACS Nano* **2013**, *7*, 3627−3634.